

RESEARCH ARTICLE

10.1002/2014JC010403

Spectral characterization of fine-scale wind waves using shipboard optical polarimetry

Nathan J. M. Laxague¹, Brian K. Haus¹, Darek Bogucki², and Tamay Özgökmen¹

¹Department of Ocean Sciences, Rosenstiel School of Marine and Atmospheric Science, University of Miami, Miami, Florida, USA, ²Department of Physical and Environmental Sciences, College of Science and Engineering, Texas A&M University, Corpus Christi, Texas, USA

Key Points:

- Gravity-capillary waves provide large share of surface roughness
- Pure capillary waves contribute least to surface roughness
- Pure capillary waves are least sensitive to changes in wind speed

Correspondence to:

N. Laxague,
nlaxague@rsmas.miami.edu

Citation:

Laxague, N. J. M., B. K. Haus, D. Bogucki, and T. Özgökmen (2015), Spectral characterization of fine-scale wind waves using shipboard optical polarimetry, *J. Geophys. Res. Oceans*, 120, 3140–3156, doi:10.1002/2014JC010403.

Received 27 AUG 2014

Accepted 16 FEB 2015

Accepted article online 20 FEB 2015

Published online 28 APR 2015

Abstract Fine-scale sea surface waves are of profound importance to a number of air-sea interaction processes. Due to a number of reasons, there exists a great degree of difficulty in obtaining quality in situ observations of these waves. This paper presents the application of a shipboard wave-sensing method toward the following quantifications: regime-specific contribution to sea surface slope and sensitivity to wind speed increases. Measurements were made via polarimetric camera, resolving waves with wavelengths ranging from 0.21 to 0.003 m ($30 \text{ rad/m} < k < 1750 \text{ rad/m}$). The gravity-capillary regime was found to contribute the bulk of mean square slope during stationary wind conditions and supply the majority of mean square slope growth during periods of increasing wind speed. Capillary waves were found to contribute approximately 5% of the overall surface roughness. Furthermore, capillary waves were found to be the least sensitive to increases in wind speed. This implies that such waves saturate at low wind speeds ($\approx 3 \text{ m/s}$) and slow wind speed increases ($\approx 0.02 \text{ m/s}^2$). The slight roughness contribution from capillary waves and significant contribution from gravity-capillary waves offers insight for scientists in the remote sensing field and important information for the formation of new wave models.

1. Introduction

Gravity-capillary and capillary waves play an integral role in many physical processes by which the atmosphere interacts with the ocean. Their short-scale undulation of the water surface enhances gas flux [Frew *et al.*, 2004; Hara *et al.*, 1998], facilitates the transfer of momentum between wind and waves [Plant, 1982], and allows ocean surface features to be remotely sensed via microwave radar systems [e.g., Jackson *et al.*, 1992; Wright, 1978; Donelan and Pierson, 1987; Hwang *et al.*, 1996; Romeiser *et al.*, 1997]. Vandemark *et al.* [2004], following earlier works, noted that gravity waves ($\lambda > 30\text{cm}$) are assumed to account for 20%–30% of all mean square slope, leaving a large share in the gravity-capillary and capillary scales. Previously, Phillips [1985] stated as part of his investigation of wave spectra that short waves (although not capillary waves, which were not considered in that paper) contribute heavily to sea surface slope. Hwang [2005] repeated the well-established assertion that decimeter to centimeter short gravity and gravity-capillary waves (specifically, those in the so-called intermediate range, $1 \text{ rad/m} < k < 316 \text{ rad/m}$) were the greatest contributors to overall sea surface slope variance. Within that discussion, the author invoked a working hypothesis that capillary waves may not contribute significantly to the mean square slope of the ocean surface, following a statement to that effect from Plant [1982]. To wit: “. it has been speculated that capillary waves may not contribute a significant portion to the ocean surface mean square slope but a definitive proof remains unavailable.” In that same paper, the theoretical results of Wentz [1976] were cited, in particular, that the sun glint measurements of Cox and Munk [1954] serve only as a lower bound for the mean square slope of the ocean surface. Methods which target a particular wavenumber regime are typically employed to infer total mean square slope because of the difficulty in measuring the bandwidth; Jackson *et al.* [1992] presented mean square slope measurements that were obtained from the ROWS k_r -band altimeter. Those values, although lower and less wind-sensitive than the densitometer-obtained results of Cox and Munk [1954], have been useful in the characterization of the sea surface over a variety of wind conditions. In spite of the fact that the body of roughness and short-wave data has grown considerably since the time of Cox and Munk's work, recent studies of this topic [Bringer *et al.*, 2013; Caulliez and Guérin, 2012] have underlined the need for further observation of gravity-capillary and capillary waves, especially in the field. Bringer *et al.*

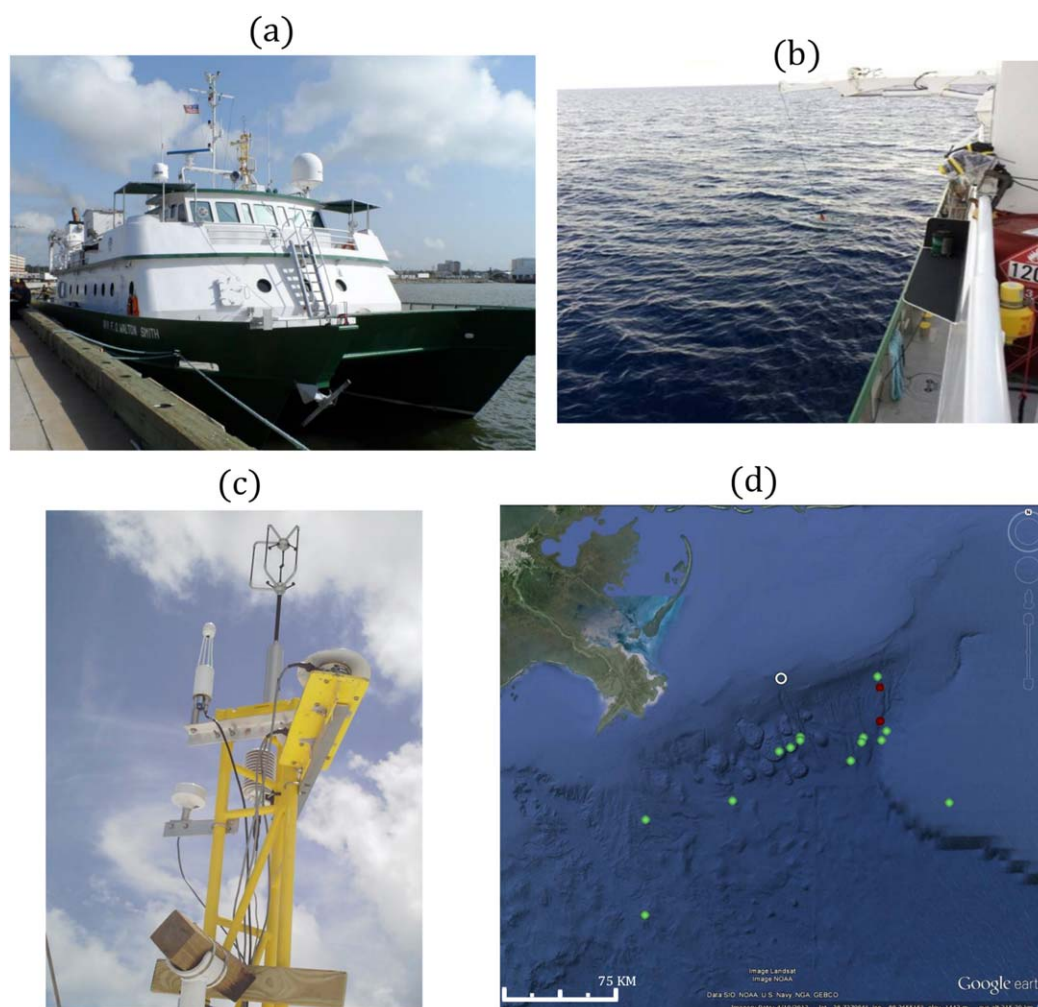


Figure 1. (a) R/V F.G. Walton Smith at dock in Gulfport, MS; (b) View of polarimeter mounted on starboard rail of 01 deck of the Walton Smith; (c) Meteorological mast mounted above pilot house; the Gill R2A sonic anemometer atop the mast served as our wind speed sensor; (d) Locations of polarimetric acquisition, GLAD. Green dots represent areas used in the stationary wind forcing analysis and red dots represent areas used in the nonstationary wind forcing analysis. The white annulus represents the location of NDBC buoy 42040.

[2013] noted large discrepancies between the model spectra of *Elfouhaily et al.* [1997] and *Kudryavtsev et al.* [1999] at high wavenumbers and called for the development of a new short-wave spectral model. They argued that neither the Elfouhaily nor the Kudryavtsev model described the normalized radar cross-section (NRCS) with consistency, even with the addition of an improved scattering model. In a similar vein, but to different effect, *Caulliez and Guérin* [2012] stated that new spatial wave measurements are needed in order to characterize sea surface statistics, especially those which seek to describe the structure and geometry of the ocean surface.

Due to the small amplitude and short wavelength of these waves and other characteristics (two-dimensional propagation and Doppler shifting by longer, faster waves) [*Hara et al.*, 1994], their measurement has been a difficult task in the laboratory and the field. According to *Jähne and Riemer* [1990], it is advantageous to measure the slope of the water surface as opposed to its elevation due to the smaller dynamic range of the slope signal. Given these and other considerations, *Zappa et al.* [2008] proposed a method by which the sea surface slope might be inferred from the polarization of light reflected from its surface. The polarimetric slope sensing (PSS) method offers a host of opportunities to those wishing to address scientific questions about the fine-scale structure of the ocean surface. The PSS method provides a unique mode of observation for field wave measurements that is both sensitive enough to resolve capillary waves and rugged enough to survive the motions of the observation platform. The camera apparatus has no in-water component; as

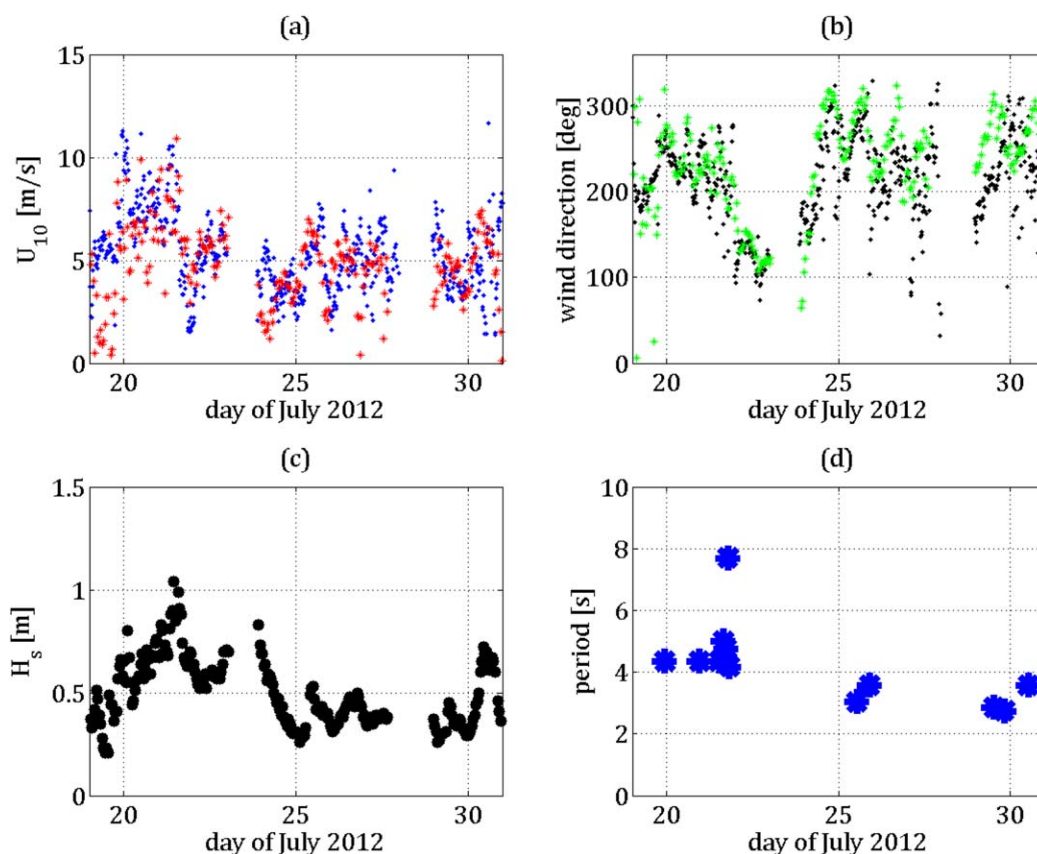


Figure 2. Wind and wave conditions in the vicinity of the ship during data acquisition. Data taken from NDBC buoy 42040 exist as 1 hour averages; wind speed and direction measurements collected aboard the *R/V F.G. Walton Smith* have been organized into 1 hour averages for this figure. (a) Blue dots indicate U_{10} as measured by the *R/V F.G. Walton Smith*; red dots indicate U_{10} as measured by NDBC buoy 42040. (b) Black dots indicate wind direction as measured by the *R/V F.G. Walton Smith*; green dots indicate wind direction as measured by NDBC buoy 42040. (c) H_s as measured by NDBC buoy 42040. (d) Dominant wave period as measured by NDBC buoy 42040 during times of polarimetric data acquisition.

such, platform effects and other distorting influences may be minimized by orienting the device sufficiently far away from the ship. The method allows for time-dependent evaluation of spatial slope spectra, enabling analysis of sea surface waves in nonstationary conditions. Field data used in this paper were collected aboard the *R/V F.G. Walton Smith* during the Grand LAgangian Deployment (GLAD), an upper-ocean drifter experiment that took place during the Summer of 2012. GLAD is discussed in greater detail within *Olascoaga et al.* [2013] and *Poje et al.* [2014].

In section 2.1, the polarimeter and accompanying sensors used during the GLAD field experiment are described. A brief introduction to the PSS method, including its general framework and the underlying theory, is presented in section 2.2. The specific application of Fourier analysis used is described in section 2.3. Results of the PSS method are studied to further investigate the behavior of the sea surface in stationary wind conditions, beginning with two-dimensional saturation spectra, omnidirectional slope spectra, and mean square slope given section 3.1. Section 3.2 shifts to an exploration of results from decidedly nonstationary wind forcing, focusing instead on naturally observed steady wind speed increases. Section 4 contains a summary of this work and a discussion of its future applications.

2. Methods

2.1. Field Observations: The GLAD Experiment

The Grand LAgangian Deployment, or GLAD, was a large-scale surface drifter experiment executed over 3 weeks in July and August of 2012 in the northern Gulf of Mexico. The entire study was part of a larger effort

by the Consortium for Advanced Research on Transport of Hydrocarbon in the Environment, or CARTHE, to better understand the transport and mixing of oil in the upper ocean. During GLAD, over 300 GPS-tracked surface drifters were released in near-simultaneous deployments. These deployments were designed to enhance the understanding of motions ranging from 100 m to 100 km in scale. In between drifter release operations, the sea surface was imaged using the rail-mounted polarimeter. The device was oriented off the starboard bow of the *R/V F.G. Walton Smith* during the experiment (Figure 1). Polarimetric data acquisition during GLAD was designed to target phenomena at the smaller spatial scales unresolved by the drifter deployment ($O(1)$ meter and smaller) but still important to upper ocean transport and mixing. It was also necessary to measure the wind forcing for a more complete characterization of the sea surface. To this end, an additional mast was installed above the pilot house for enhanced meteorological measurements. Wind speed was measured by the Gill R2 sonic anemometer. Additionally, an infrared camera was colocated with the polarimeter.

2.2. Polarimetric Slope Sensing

In order to properly observe gravity-capillary and capillary waves, it is almost always necessary to use a near-synoptic spatial data acquisition method [Hara *et al.*, 1994; Hwang, 2005]. Doppler shifting of short-scale waves by longer, faster ones is extremely difficult to quantify. Researchers have attempted to work around this issue by equipping a free-drifting buoy with wave gauges [Hwang, 2005]. The methods of this paper, however, involve use of a polarimeter (in the style of Zappa *et al.* [2008]), which images the sea surface, gathering spatial data in a functionally synoptic fashion. This sensor encloses a single lens, a beamsplitter, and three CCDs that each acquire images of 640 by 480 pixels at 54 Hz (integration time of 16.56 ms) in one of the following three linear polarization states: 0, $\pi/2$, and π . The concluding section of Zappa *et al.* [2008] states that, in the presence of ocean swell, an integration time of less than 0.1 ms is needed to avoid motion blur in the capillary waves. Visual inspection of the camera images did not reveal any perceptible amount of motion blur. While no direct measure of swell presence was made aboard the *R/V F.G. Walton Smith*, the wave information pulled from a nearby NDBC buoy (#42040) indicates that swell was either minimal or absent throughout the bulk of the experiment. Specifically, the dominant wave period only surpassed 4 s once during camera acquisition and H_s remained below 1 m throughout the experiment, hovering around 50 cm during most of the cruise (Figure 2). Polarimetric data acquisition was never executed within 80 km of the shore, allowing for sufficiently large fetch regardless of wind direction. Wind speed, wind direction, and peak wave direction are also plotted in Figure 2; a great degree of spatial uniformity was found in the wind field, owing to the agreement in wind speed magnitude and direction despite the ship and buoy separation of 50–100 km throughout the experiment. The ship-based wind data were used in all of the analysis that follows.

Before processing, each frame is projectively transformed to the ocean surface plane and trimmed to a 640 by 640 pixel image. Intensity information outside of this range is not considered. Due to the camera acquisition angle of 49° below the horizontal, features at the top of each image are stretched more than those at the frame's bottom. This may cause noise to contaminate the intensity data at different scales across the sampling region, however, such a process is necessary for maintaining a homogeneous spatial scale (≈ 0.001708 m/px) across the image. While the effects of the ship's motion were not directly taken into consideration for this projection, calculation revealed that the pixel resolution varies by less than 9% for 5° pitch and roll (the maximum pitch and roll observed during the experiment). Subpixel information is lost by the cameras, however, preventing resolution below the Nyquist wavenumber of ≈ 1750 rad/m (minimum resolvable scale of ≈ 3.59 mm). In Zappa *et al.* [2008], the authors make use of simplified Müller calculus to interpret the images taken from a camera apparatus able to simultaneously acquire in three different linear polarization states (here 0, $\pi/2$, and π , as seen in Figure 5).

The light intensities as measured by the cameras are used in the explicit determination of the Stokes parameters. These parameters form elements of the Stokes vector).

$$\begin{aligned} S_0 &= I_0 + I_{\pi/2} \\ S_1 &= I_0 - I_{\pi/2} \\ S_2 &= 2I_{\pi/4} - S_0 \end{aligned} \quad (1)$$

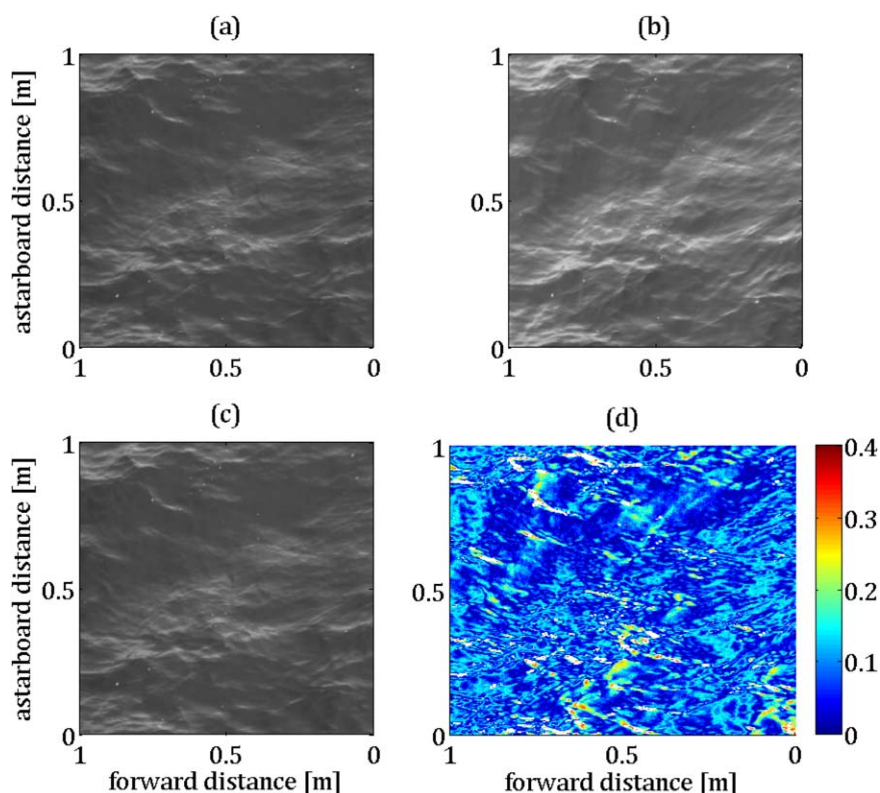


Figure 3. (a) Camera frame, $\pi/4$ polarization, (b) camera frame, π polarization, (c) camera frame, 0 polarization, and (d) computed slope field.

I_0 , $I_{\pi/4}$, and $I_{\pi/2}$ are the light intensities at 0, $\pi/4$, and $\pi/2$ radians, respectively. From two of these Stokes parameters, S_1 and S_2 , it is possible to compute the polarization orientation Φ . This value is $\pi/2$ from φ , the angle made by the intersection of the plane of reflection and the image plane.

$$\Phi = \frac{1}{2} \arctan\left(\frac{S_2}{S_1}\right) \quad \varphi = \Phi + \frac{\pi}{2} \tag{2}$$

From Müller calculus, it is possible to determine the reflective properties of the surface from the Stokes parameters. Specifically, with the assumption that upwelling radiation may be neglected, one may obtain a relation between the degree of linear polarization, or DOLP, and the Fresnel reflection coefficients r_{\parallel} and r_{\perp} . In short, this gives the user the ability to relate the computed Stokes parameters to the angle of incidence of the observed light. For diffuse (that is, nonlocally concentrated), uniform illumination of the air-sea interface, this angle of incidence is in fact the orientation of the reflecting surface with respect to the camera.

$$DOLP(\theta, n) = \sqrt{\frac{S_1^2 + S_2^2}{S_0^2}} = \frac{r_{\parallel}^2 - r_{\perp}^2}{r_{\parallel}^2 + r_{\perp}^2} \tag{3}$$

$$r_{\parallel} = \frac{\tan(\theta_i - \theta_t)}{\tan(\theta_i + \theta_t)} \quad r_{\perp} = \frac{\sin(\theta_i - \theta_t)}{\sin(\theta_i + \theta_t)} \quad \theta_i = n \sin(\theta_t) \tag{4}$$

With these two angles, incidence and polarization orientation, one may define the slope in two dimensions for each point. The result of these computations is (for each triplet of synchronous frames) a two-dimensional slope field; that is, an array of slope vectors $\vec{\sigma}(x, y)$ defined at each image pixel. The corresponding spatial resolution is determined by the number of pixels, the camera's location with respect to the water surface, and the lens used. Chief among the assumptions made in these calculations are the following: that the light incident on the water surface is unpolarized and that upwelling radiation is negligible. These assumptions were found to be appropriate for many conditions during the GLAD experiment.

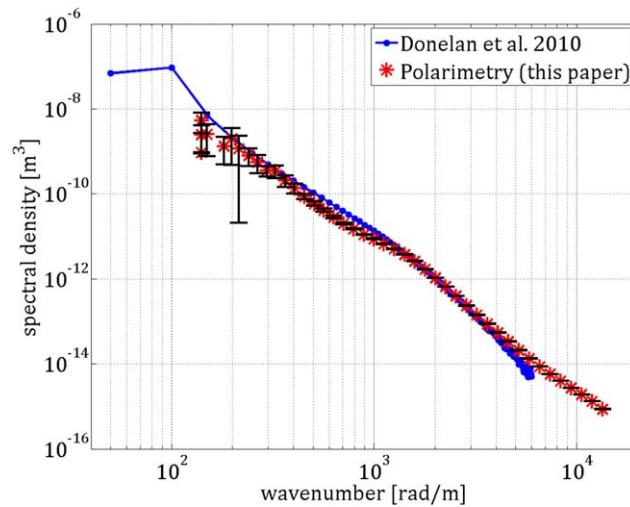


Figure 4. Comparison of elevation spectra produced from the polarimeter and the wavelet directional method (WDM) results from *Donelan et al.* [2010] within ASIST. Red asterisks represent the polarimetric spectrum and the blue line represents the WDM spectrum; black error bars about the polarimetric data points indicate 95% confidence intervals. Wind speed condition: $U_{flume} = 5.0$ m/s at $z = 30$ cm ($U_{10} = 7.6$ m/s).

2.3. Spectral Analysis

The spatial Fourier transform of the two-dimensional slope fields will yield information about the directional distribution of energy within that imaged area of the water surface. For this paper, $x(k_x)$ represents displacement (magnitude in wavenumber space) forward along the longitudinal axis of the ship. Similarly, $y(k_y)$ represents displacement (magnitude in wavenumber space) off the starboard bow. Given a two-dimensional slope magnitude array $\sigma(x, y) = \|\vec{\sigma}(x, y)\|$, where $\vec{\sigma}(x, y)$ is the two-dimensional slope vector field defined at location on the water surface (x, y) , one may compute its corresponding two-dimensional wavenumber slope spectrum $P(k_x, k_y)$, with dimensions of meters squared. The symbol δ represents the camera's spatial resolution in meters per pixel.

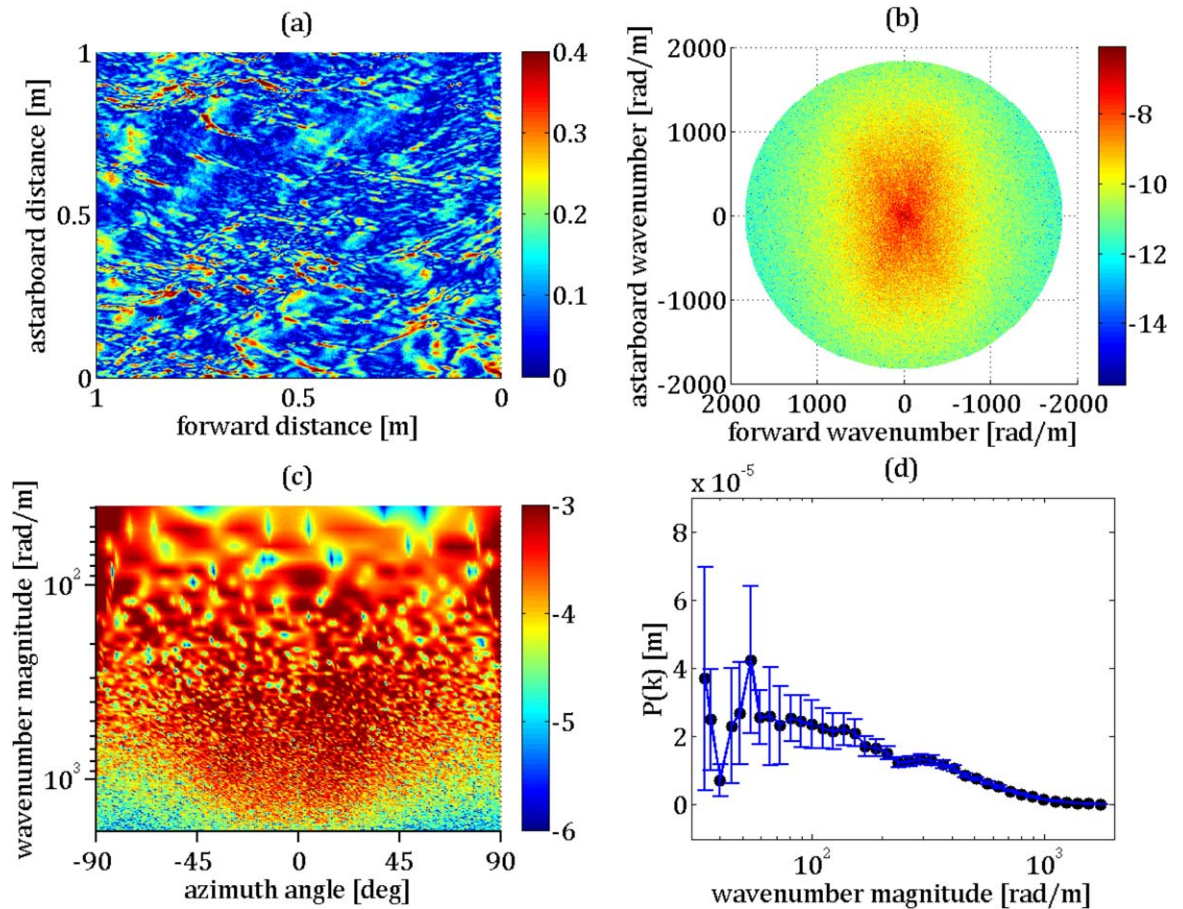


Figure 5. (a) Computed slope field from Figure 3d, (b) 2-D slope spectrum, (c) 2-D saturation spectrum oriented about wind direction, in the style of *Jähne and Riemer* [1990], (d) omnidirectional slope spectrum $P(k)$. Error bars indicate 95% confidence intervals.

$$A = \int_{-\infty}^{+\infty} \int_{-\infty}^{+\infty} e^{i(k_x x + k_y y)} \sigma(x, y) dx dy, P(k_x, k_y) = \frac{|A|^2}{N k_{max}^2} \tag{5}$$

where N is the number of data points and $k_{max} = \frac{2\pi}{\delta}$

$$P(k) = \int_0^{2\pi} k P(k_x, k_y) d\theta = k P(k_x, k_y) \int_0^{2\pi} d\theta = 2\pi k P(k_x, k_y) \tag{6}$$

where $k = \sqrt{k_x^2 + k_y^2}$ and P(k) is the omnidirectional slope spectrum. P(k) is alternatively equivalent to $k^2 S(k)$, where S(k) is the omnidirectional elevation spectrum. The mean square slope may be computed by integrating the slope spectrum over a desired wavenumber range. This property will be taken advantage of as the paper progresses. The two-dimensional saturation spectrum $B(k_x, k_y)$ is a dimensionless spectrum commonly used in the study of gravity-capillary and capillary waves. This may be alternatively represented in a form convenient for these purposes as $k^2 P(k_x, k_y)$.

2.4. Laboratory Validation

In order to validate our execution of the PSS method and the associated spectral analysis, supplementary polarimetric data were collected in the Air-Sea Interaction Saltwater Tank (ASIST) facility. The same camera used during GLAD was operated above the wave tank. The same acquisition and processing codes were employed. For reasons described in section 1, it is difficult to correctly describe fine-scale surface features using a point elevation gauge and traditional time series analysis. As a result, the wavenumber spectra computed in *Donelan et al.* [2010] were chosen for comparison. The data that produced those spectra were obtained in the ASIST facility (at the same fetch as the polarimeter data) from colocated point slope and elevation gauges and processed using the Wavelet Directional Method (WDM) of *Donelan et al.* [1996]. The WDM makes use of the phase difference in measurements between closely-positioned wave gauges in order to obtain spatiotemporal information about the wave field. In *Donelan et al.* [2010], the colocated point slope and elevation time series data described the first two terms of a Taylor series about the measurement location; this produced four virtual wave staffs ($\delta = 0.01$ mm separation). A stage in the WDM process involves the application of a wavenumber vector to each particular frequency band throughout the time series, resulting in a wave observation method that accounts for the Doppler-shifting effects of long-wave advection. A single condition, corresponding to U_{10} of 7.6 m/s, was selected as it was the only wind speed case that corresponded with the laboratory-obtained polarimetry and fell within the measured range of wind speeds from GLAD. Figure 3 displays the WDM-produced omnidirectional elevation spectrum alongside the corresponding polarimetric spectrum $S(k) = k^{-2} P(k)$. The spectra agree well across wavenumbers ranging from 150 rad/m to 6000 rad/m despite the fact that the data were not obtained simultaneously.

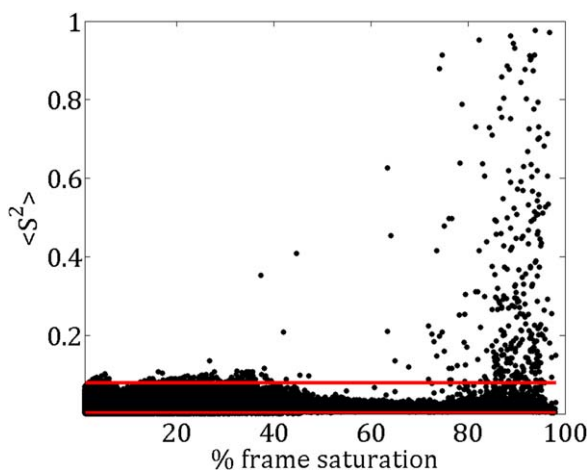


Figure 6. Variation of mean square slope with respect to percent image saturation. The vertical axis represents mean square slope; the horizontal axis represents the percent saturation (percent of frame with pixel values = 255) in the brightest of the three polarimetric images. The minimum and maximum mean square slope values for the observed wind speed range (as computed via the linear fits of *Cox and Munk* [1954]) are given.

2.5. Quality Control and Data Selection

2.5.1. Preliminary Quality Control

In order to reduce the effect of glint-based image saturation on the slope measurements, instances in which one of the three frames saw more than 50% of the image saturated with brightness were not used for calculations. Sun glint-contaminated frames (saturation >50%) account for less than 1% of the total images captured. Furthermore, Figure 4 shows some of the nonphysical MSS values that may be obtained from glinty frames. In a similar vein, only those times during which the wind originated from bow to stern on the starboard side were considered during

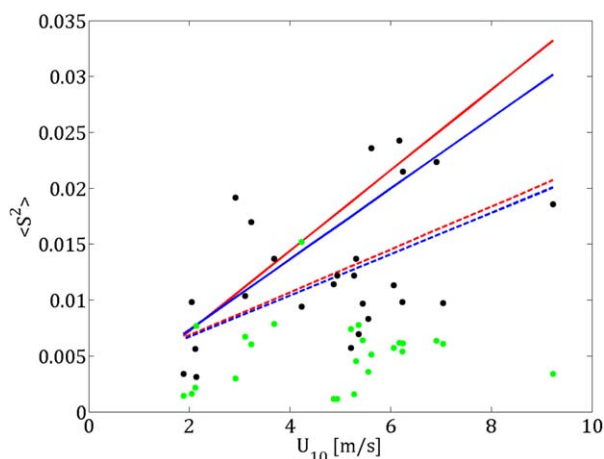


Figure 7. Mean square slope plotted against wind speed. The black and green dots represent the polarimeter-obtained along and cross-wind mean square slope, respectively. The red solid and dashed lines represent the linear fits for along and cross-wind (respectively) from *Cox and Munk* [1954] and *Cox and Munk* [1956]. The blue solid and dashed lines represent the linear fits for along and cross-wind (respectively) from *Br on and Henriot* [2006].

slope computation. Through these methods of quality control, the effect of the measurement platform on the measurements themselves is minimized. Additionally, there is a reduction in the incidence of spurious wave slope values calculated from significantly saturated frames. Unfortunately, the high temporal resolution six degree-of-freedom motion package failed during the experiment, so direct covariance measurements were not possible. This failure also hampered motion-dependent image rectification of polarimeter frames, making frame-by-frame analysis and comparison all but impossible. For this reason, polarimeter results are presented either over reasonably long averaging times (stationary cases) or as linearized rates of change (nonstationary cases). For better comparison with other results, wind speed measurements were referenced to their

corresponding 10 m neutral values using the method of *Smith* [1988]. During an evaluation of the effects of this method on the data set, the difference between the 10 m referenced values and the 11.4 m measured values was found to be negligible ($\approx 1\%$) for all wind conditions.

2.5.2. Data Selection: Stationary Wind Forcing

Traditional wave spectral analysis requires stationary wind forcing (which is to say wave) conditions. For an appropriate comparison, the presentation of results begins with a focus on periods of quasi-stationary

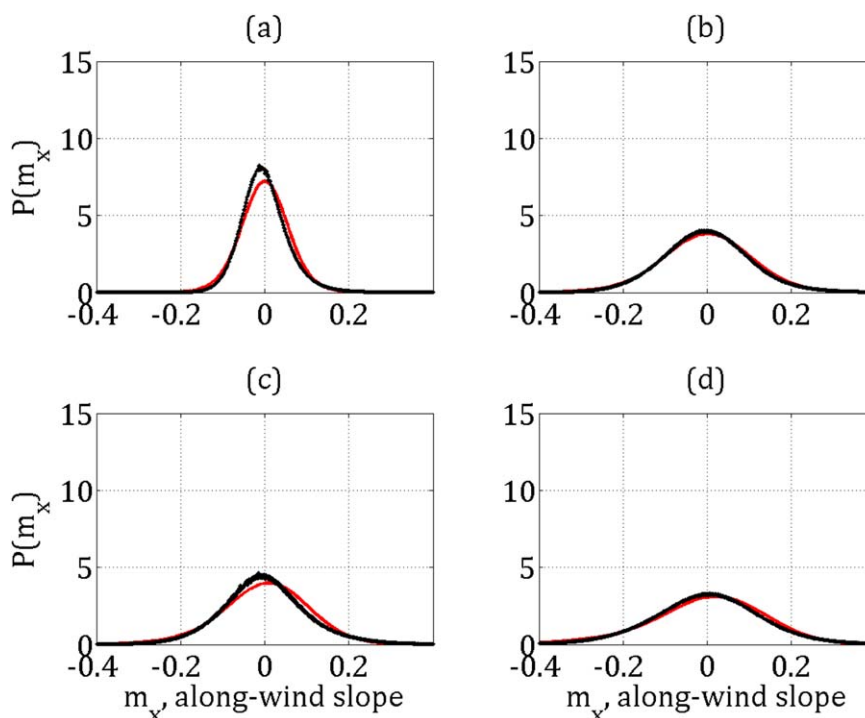


Figure 8. Along-wind slope distributions from four reasonably-spaced wind speed conditions. $U_{10} =$ (a) 1.888 m/s, (b) 4.941 m/s, (c) 7.039 m/s, and (d) 9.225 m/s. The black dots represent the polarimeter-obtained slope distributions; the red lines represent the Gram-Charlier-modified Gaussians used by *Cox and Munk* [1954] and *Cox and Munk* [1956]. The parameters of that expansion were provided by *Br on and Henriot* [2006], with mean square-slope values provided by the polarimeter.

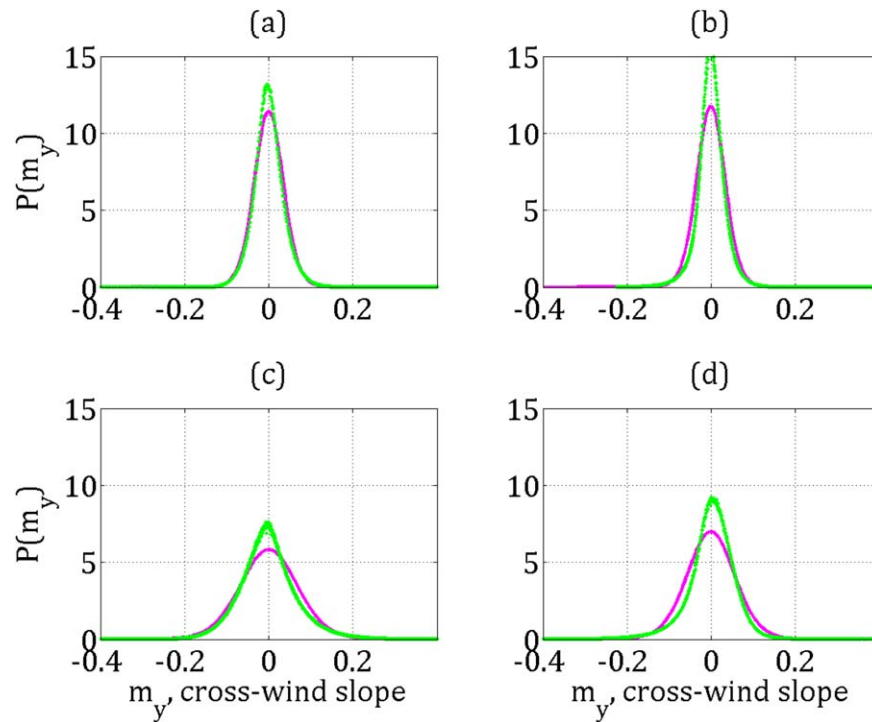


Figure 9. Cross-wind slope distributions from four reasonably-spaced wind speed conditions. U_{10} = (a) 1.888 m/s, (b) 4.941 m/s, (c) 7.039 m/s, and (d) 9.225 m/s. The green dots represent the polarimeter-obtained slope distributions; the magenta lines represent the Gram-Charlier-modified Gaussians used by Cox and Munk [1954] and Cox and Munk [1956]. The parameters of that expansion were provided by Bréon and Henriot [2006], with mean square-slope values provided by the polarimeter.

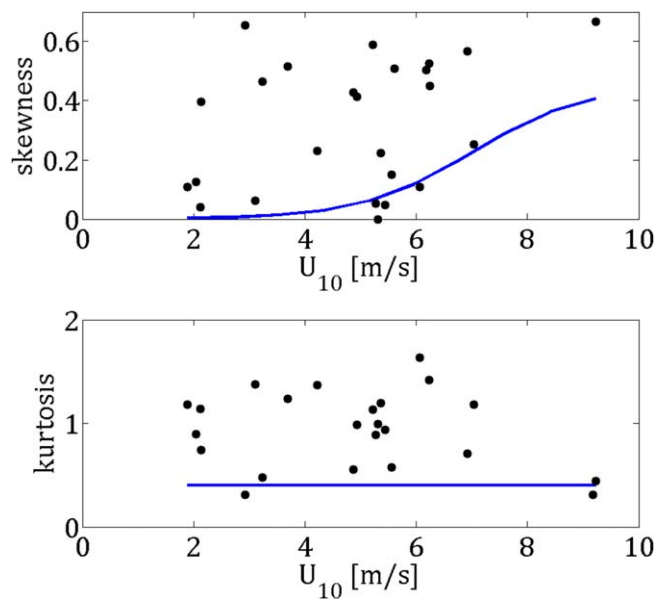


Figure 10. Along-wind skewness and kurtosis (peakedness) in the style of Cox and Munk [1954] and Cox and Munk [1956]. Following those works, the skewness parameter $c_{30} = \langle \zeta^3 \rangle$ and the kurtosis (peakedness) parameter $c_{40} = \langle \zeta^4 \rangle - 3$, where ζ is the wave slope normalized with respect to the root mean square slope, i.e., $\zeta = m_x / \sigma_x$. The black dots represent polarimeter-measured values; the blue lines represent the fits as obtained by Bréon and Henriot [2006].

winds within the GLAD experiment. For this purpose, it was necessary to select relevant time intervals with consistency and to maintain as high a level of quality control as the field allowed. Intervals no shorter than 1 min during which the measured wind speed was shown to be stationary were considered here. These periods are hereafter referred to as “cases” for brevity. Stationarity was evaluated using the Augmented Dickey-Fuller (ADF) test. The ADF test has been shown to outperform other methods in the stationarity evaluation of simulated time series data [Choi, 2001]. In order to minimize the distorting effects of the ship on the measurements, cases with unfavorable wind direction conditions were neglected. Specifically, those times during which the wind direction was oriented on the port side (leaving the polarimeter footprint on the water sheltered by the ship)

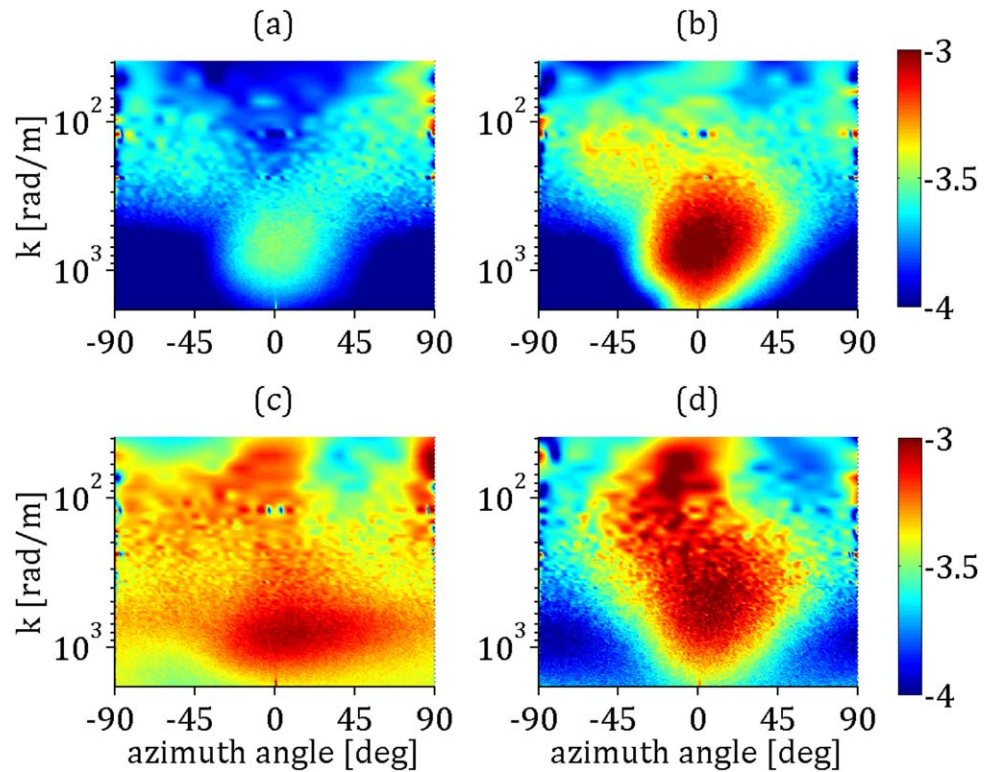


Figure 11. Two-dimensional saturation spectra, four selected stationary cases. U_{10} = (a) 4.228 m/s, (b) 4.941 m/s, (c) 6.175 m/s, and (d) 9.225 m/s.

were removed from consideration. Due to the high rate of data transfer through the board, the incidence of drop-outs was prevalent; cases for which 99% or more of a sample's frames were nonexistent were ignored in order to maintain an acceptable level of data points for averaging purposes.

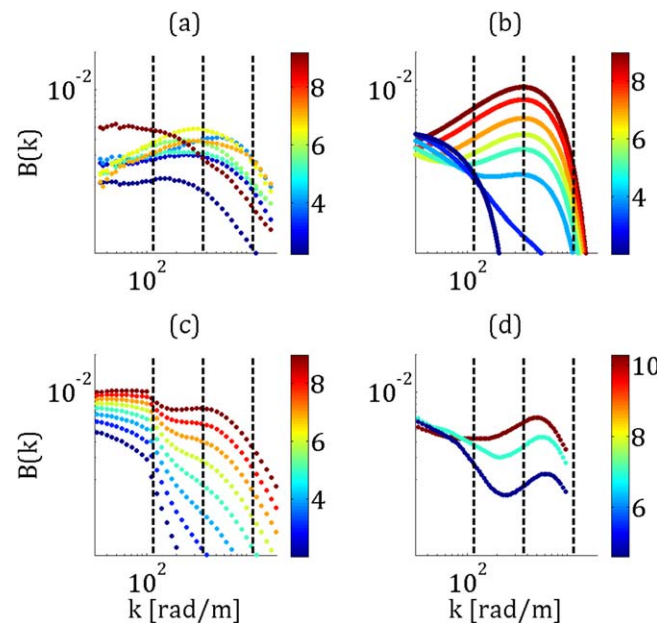


Figure 12. Omnidirectional saturation spectra. Color indicates U_{10} in m/s. Dashed lines demarcate the four regimes described in Table 1. (a) Polarimetric data from this study, (b) spectrum of *Elfouhaily et al.* [1997], (c) spectrum of *Hwang* [2011], and (d) field-derived spectra of *Yurovskaya et al.* [2013].

2.5.3. Data Selection: Nonstationary Wind Forcing

Spectral analysis of ocean surface waves measured by traditional, time-series wave gauges requires stationary conditions over the sample duration (typically 5–60 min). The polarimeter used in this study allows for evaluation of high-wavenumber directional wave spectra, omnidirectional wave spectra, and integral moments (for the purpose of this paper, mean square slope) in nonstationary conditions because it uses the 2-D spatial structure derived from single images. For the purposes of this study, focus has been directed to periods of uniformly increasing wind speeds ($\frac{\partial^2 U}{\partial t^2} \approx 0$); in a word, “ramps.”

While constraining attention to periods exhibiting this behavior neglects a good deal of interesting phenomena, it provides an excellent platform for careful study of nonstationary wind forcing

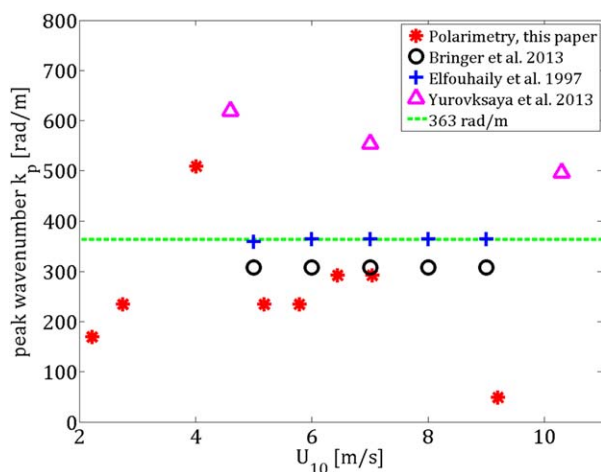


Figure 13. Short-wave peak wavenumbers, omnidirectional saturation spectra. Red asterisks represent the results of this paper; black circles represent peak wavenumbers from the Bringer *et al.* [2013] spectra; blue plus-signs represent peak wavenumbers from the Elfouhaily *et al.* [1997] spectra; magenta triangles represent peak wavenumbers from the observation-derived spectra of Yurovskaya *et al.* [2013]. The green line indicates 363 rad/m, the short-wave peak used in Elfouhaily *et al.* [1997] and many other works.

with the roughness observed in the polarimeter's approximately 1 m² footprint. For this reason, a method was chosen that focused on nearly-linear wind speed increases of longer time scales (50–500 s). The filters applied in that section aimed at the elimination of dark or saturated frames from consideration were also applied for the work mentioned here.

3. Results

3.1. Stationary Wind Conditions

The conditions defined in 2.5.2 allowed for the consideration of 26 cases representing polarimetric video acquisition during periods of quasi-stationary wind forcing. The spatial distribution of these points can be found in Figure 1d. Figures 9 and 10 give slope distributions for the stationary wind conditions. Slope distributions are shown in comparison to the modified Gaussians of Cox and Munk [1954] (and updated for Munk [2009] based on Bréon and Henriot [2006]). Results from polarimetry appear to agree with the parameterized distributions. The cumulants skewness and kurtosis are plotted in Figure 11 in comparison with the values found by Bréon and Henriot [2006]. In general, the observed polarimetric slope distributions are far more peaked (although no more wind-dependent) than those found for the previously listed works. There is a great deal of variability in observed skewness, although the paucity of data points corresponding to the so-called “critical” value $U_{10} > 7$ m/s (as in Jackson *et al.* [1992] and others) makes a proper comparison difficult. In any case, the results of prior works seem to set an approximate lower bound for the values observed here.

3.1.1. Wave Slope/Saturation Spectra

In order to evaluate the wave observations gathered by the polarimeter, it is convenient and useful to compare its measured wave spectra and associated moments with well-established model spectra and prior observations. Bringer *et al.* [2013] found the model spectrum of Kudryavtsev *et al.* [1999] to overestimate mean square curvature (MSC) and normalized radar cross-section (NRCS). Whereas the spectrum of Kudryavtsev *et al.* [1999] was based on a physical representation of the energy balance equation [Bringer *et al.*, 2013], the spectrum of Elfouhaily *et al.* [1997] drew its form from field and laboratory observations. For the comparisons presented here, the empirically founded spectrum of Elfouhaily *et al.* [1997] was chosen because of its incorporation of available field measurements in the high wavenumber domain sensed by the polarimeter. Additionally, the parameterized spectrum of Hwang [2011] and the field-obtained spectra of Yurovskaya *et al.* [2013] have been included for perspective. The spectrum presented in Bringer *et al.* [2013] is considered in later sections, but its discontinuities at lower wind speeds prevent direct comparison for many of the conditions observed here.

To display the individual spectra from all the cases chosen would be prohibitively space-consuming; as a result, this section will focus on condensing their information into more readily understandable graphics. For reference, an example two-dimensional saturation spectrum is given in Figure 6c. The seemingly spurious off-wind values at

outside the laboratory environment. In a style similar to that of the process described in section 2.5.2, individual “cases” were isolated by their adherence to a simple model: nearly-linear increase in wind speed with stationary (and favorable) wind direction. Due to the reasonably large separation between the anemometer and the ocean surface (11.4 m), there exists a degree of ambiguity preventing the comparison of any single gust to a corresponding change in surface roughness. Flux footprints of $\approx 3.2 \cdot 10^5$ m² have been observed at a measurement height of 10 m above the mean water level [Högström *et al.*, 2008]. It is difficult to say with any degree of certainty whether a quick change in wind conditions would be directly associated

around 100 rad/m are artifacts of the interpolation required to project the semicircular spectrum onto a square grid. They do not have any noticeable effect on the omnidirectional spectra (see Figure 6d). A more detailed (and time-averaged) version of the 2-D saturation spectrum may be found in Figure 7. No detailed analysis of the directional spreading has been performed; however, this is a rich topic that deserves further time and study in the future. In the style of Figure 9 from *Jähne and Riemer* [1990] and Figure 8 from *Hara et al.* [1998], Figure 112a in this paper gives the omnidirectional saturation spectra for each wind speed case. The other Figures 12b–12d correspond to *Elfouhaily et al.* [1997], *Hwang* [2011], and *Yurovskaya et al.* [2013], respectively. The polarimetric spectra show a degree of variability, especially in low wind conditions. It is possible that surfactant plays a role in this variability, due to the likelihood of large variability in surface film conditions across sampling locations. *Frew* [1997] demonstrated that surfactant strongly dampens sea surface roughness (and therefore inhibits air-sea gas transfer) at low wind speeds. No independent measure of surfactant was made, however, so a quantitative analysis is impossible. While the spectra in Figure 12a do not fall off at centimeter scales at low winds as in the *Elfouhaily et al.* [1997] (Figure 1212b) or *Hwang* [2011] (Figure 12c) spectra, they seem to agree with *Hwang* [2011] and *Yurovskaya et al.* [2013] (Figure 12d) in the post peak spectral shape. Furthermore, the peak wavenumbers of the polarimetric saturation spectra (Figure 13) nearly all fall below the 363 rad/m used in *Elfouhaily et al.* [1997], in fair agreement with *Bringer et al.* [2013] over the range of 5–7 m/s. While the figures referenced are appropriate visualizations of the distribution of energy in each observed sea state, further work must be done to draw quantitative conclusions from these data. In order to better understand the behavior, it is necessary to focus on the wave regime-specific contributions to mean square slope.

3.1.2. Mean Square Slope

In this section, the subject of discussion shifts to the contributions to overall mean square slope by specific wave regimes. Rather than using wavenumber bands determined by remote-sensing wavelengths or some

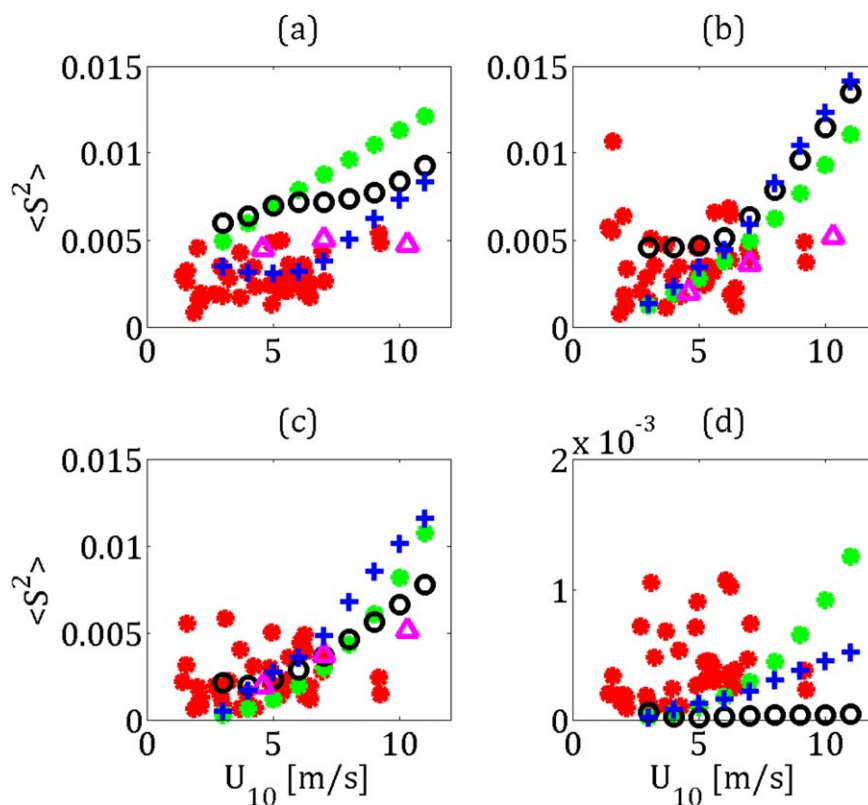


Figure 14. Mean square slope computed over four wavenumber regimes: (a) $37.1 < k < 117.1$, (b) $117.1 < k < 371$, (c) $371 < k < 1173$, and (d) $1173 < k < 1750$. Red asterisks represent polarimetric data from this study, blue plus-signs represent the integrated spectrum of *Elfouhaily et al.* [1997], black circles represent the integrated spectrum of *Bringer et al.* [2013], green asterisks represent the integrated spectrum of *Hwang* [2011], and magenta triangles represent data gathered from the integration of the *Yurovskaya et al.* [2013] field-derived spectra.

Table 1. Classification of Regimes by Wavenumber Range

Wavenumber Range	Classification
37.1 rad/m < k < 112.7 rad/m	Short gravity waves
112.7 rad/m < k < 371 rad/m	Gravity-capillary waves, part one
371 rad/m < k < 1173 rad/m	Gravity-capillary waves, part two
1173 rad/m < k < 1750 rad/m	Pure capillary waves

other metric, regimes are identified by their dominant restoring forces. To wit—short gravity, pure capillary, and gravity-capillary waves correspond to primary restoring forces of gravity, surface tension, and a mixture of the two, respectively. For the purposes of this study, four regimes spanning from

$k = 37.1 \text{ rad/m}$ to $k = 1750 \text{ rad/m}$ (k_{Nyq}) have been chosen for further study. They are as follows: short gravity ($37.1 < k < 117.3$), gravity/gravity-capillary ($117.3 < k < 371$), gravity-capillary/capillary ($371 < k < 1173$), and pure capillary ($1173 < k < 1750$). At $k = 117.3 \text{ rad/m}$, the linear dispersion relation's gravity term is an order of magnitude larger than its capillary term. At $k = 1173 \text{ rad/m}$, the converse is true. These definitions are also shown in table 1.

The breakdown of mean square slope contributions from the four, previously-mentioned regimes is shown in Figure 14. Over all wind speed ranges, the two gravity-capillary regimes (Figures 14b and 14c) together contribute the most to overall mean square slope and appear to be the most sensitive to wind speed. This is in slight contrast to the mean square slope values computed from the *Hwang* [2011] and *Bringer et al.* [2013] spectra, especially at low winds. The polarimetrically sensed short gravity wave band of $37.1 \text{ rad/m} < k < 117.3 \text{ rad/m}$ (a) excludes a great deal of the sea surface gravity wave regime, so care should be taken before one performs a direct comparison to other data, although results show agreement with the mean square slope estimates from the *Elfouhaily et al.* [1997] spectrum. The polarimetrically sensed pure capillary wave regime of $1173 \text{ rad/m} < k < 1750 \text{ rad/m}$ (d), extends sufficiently far into high-wavenumber space that it may be compared with virtually any historical capillary wave measurements. Although observed capillary-regime mean square slope values are higher than those produced from the other spectra referenced here, they are still far and away the slightest contributors to overall roughness, accounting for approximately 5% of mean square slope on average. This result seems to confirm the earlier-referenced statement contained in *Hwang* [2005] following *Jackson et al.* [1992], *Walsh et al.* [1998], and *Vandemark et al.* [2004]. Another method of examining the wavenumber dependence of mean square slope over a variety of wind speeds involves calculating their cumulative value over some sliding wavenumber range. Figure 15 shows the cumulative mean square slope

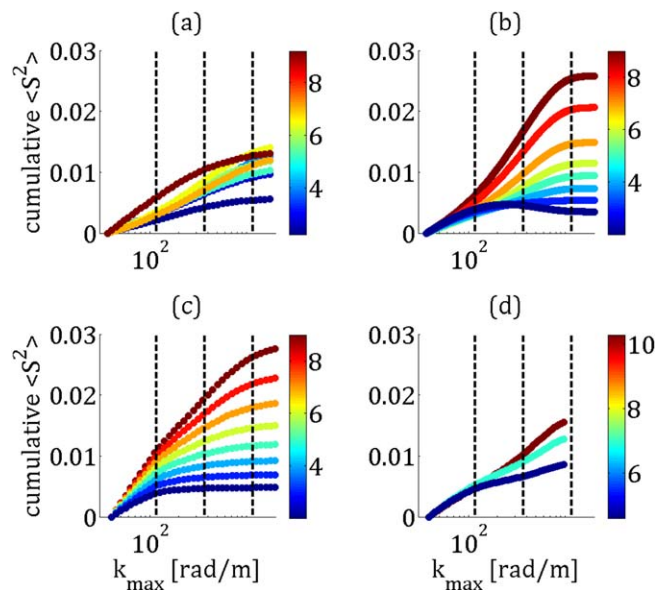


Figure 15. Cumulative mean square slope. Color indicates U_{10} in m/s. Dashed lines demarcate the four regimes described in Table 1. (a) Polarimetric data from this study, (b) integrated spectrum of *Elfouhaily et al.* [1997], (c) integrated spectrum of *Hwang* [2011], and (d) integration of the *Yurovskeya et al.* [2013] field-derived spectra. High cutoff wavenumber k_{max} is the upper limit of integration for the mean square slope computation $Cumulative \langle S^2 \rangle = \int_{37.1}^{k_{max}} P(k) dk$.

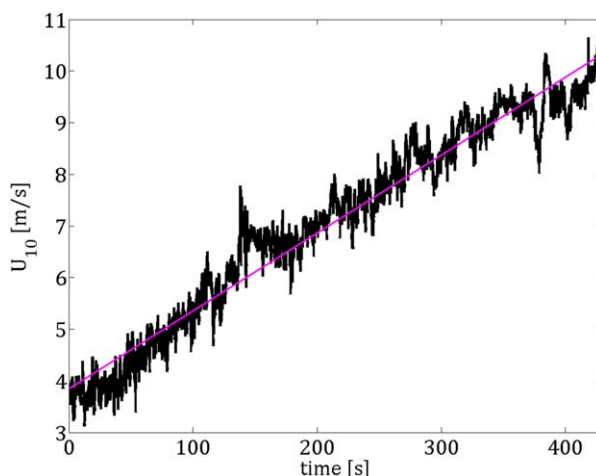


Figure 16. Wind speed, selected ramp case. $\langle \frac{\partial U}{\partial t} \rangle \approx 0.0236 \text{ m/s}^2$.

produced from polarimetry and the three outside sources used in Figure 12. The high wavenumber cutoff k_{max} represents the upper limit of integration for which the mean square slope was computed, i.e.,

$$Cumulative \langle S^2 \rangle = \int_{37.1}^{k_{max}} P(k) dk \tag{7}$$

where the wavenumber value of the lower limit of integration is, as before, 37.1 rad/m. Figure 15 shows a roughness separation between wind speeds that rapidly widens in the two interior, gravity-capillary regimes. A tapering off in the pure

capillary regime is found consistently throughout the shown examples, displaying that wave regime’s miniscule roughness contributions as seen directly in Figure 14.

3.2. Nonstationary Wind Conditions

Following the identification of several instances functionally similar to the ramp model, the field was pared down to 25 cases after quality control and an imposition of the conditions listed in section 2.5.2. While data from all such periods is used in this paper (e.g., Figure 19), the case with the longest duration is shown in Figure 16, with associated plots following in Figures 17 and 18.

3.2.1. Wave Slope Spectra

In order to properly visualize the wind’s effect on the wave spectrum, an approach different to the one taken in section 3.1 must be taken. Rather than average over the span of a period of wind stationarity, it is necessary to represent the shift of the sea state as the wind forcing conditions change. The spectrogram is a well-established visualization tool used in the study of dynamic processes. Because the

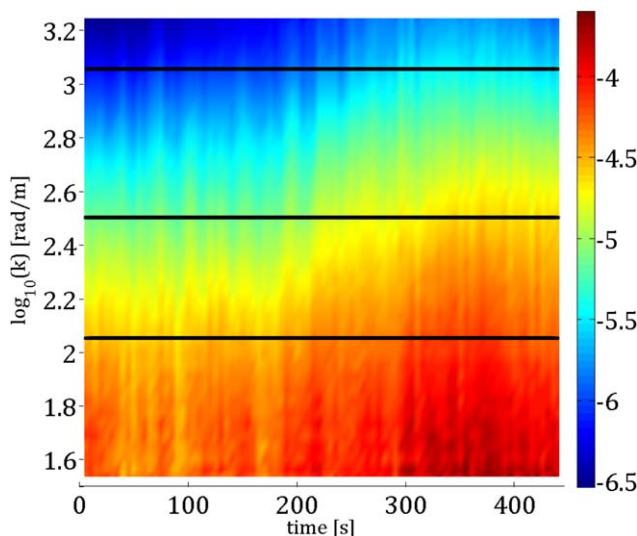


Figure 17. Wavenumber slope spectrogram corresponding to wind speed conditions plotted in Figure 16. Solid lines demarcate the four regimes described in Table 1. Plot represents the change of the shape and overall energy of the omnidirectional slope spectra during the selected ramp case, with color corresponding to (dimensionless) omnidirectional degree of saturation.

polarimeter-derived spectra may be computed in such a short amount of time, the spectrogram windows may be as short as 17 ms. Five seconds was chosen in order to reduce visual clutter and to minimize the effect of ship motions while preserving the nonstationary aspect of the ramps. Spectrograms for the chosen example are shown in Figure 17. A plateau appears to develop in the higher-wavenumber section of the gravity-capillary; the change in spectral shape no longer tracks the increasing wind speed.

3.2.2. Mean Square Slope

Due to the nonstationary nature of the cases considered in this section, it is difficult, if not meaningless, to compare these polarimetrically obtained mean

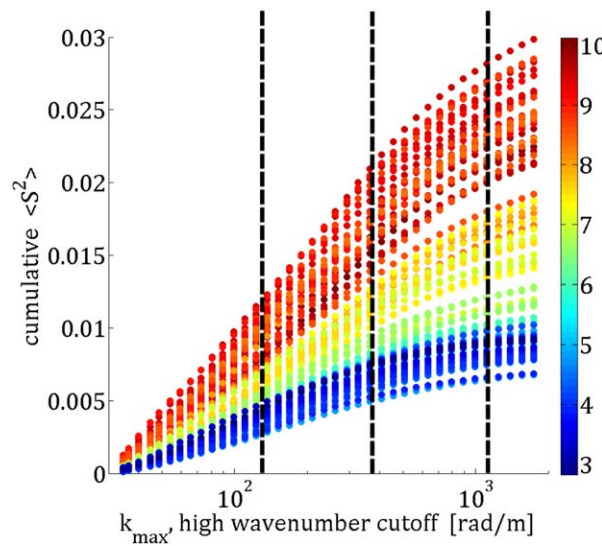


Figure 18. Cumulative mean square slope, selected ramp case. Dashed lines demarcate the four regimes described in Table 1. High cutoff wavenumber k_{max} is the upper limit of integration for the mean square slope computation $Cumulative \langle S^2 \rangle = \int_{37.1}^{k_{max}} P(k)dk$.

pure capillary regimes ($k > 700$ rad/m). This seems to coincide with the change in shape of the omnidirectional curvature spectra computed from stationary wind conditions and shown in Figure 12a, which are similar in nature to Figure 12c (Hwang [2011] spectra) and Figure 12d (Yurovskaya et al. [2013] spectra). This is not an entirely surprising result; the laboratory-derived spectra shown in Figure 9 of Jähne and Riemer [1990] also exhibit similar behavior in the high-wavenumber regime.

In keeping with the linear model used for this section, one may simply examine the rates of change of regime-specific mean square slope, framing the problem in a manner akin to the work discussed in section 3.1. This approach involves the computation of rates of change of mean square slope and rates of change of wind speed, as in Figure 19. The two intervals encompassing the gravity capillary regime show strong sensitivity to changes in wind forcing. This echoes the behavior found in the stationary study; similarly, the near-static behavior of roughness rates in the pure capillary regime brings to mind the observed mean square slope values in stationary wind forcing conditions.

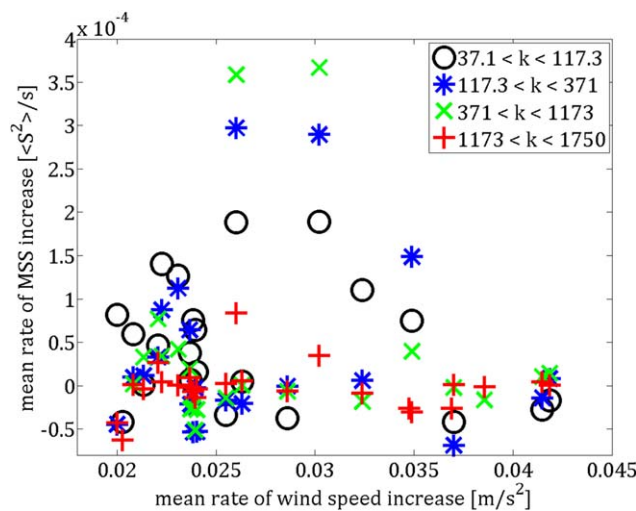


Figure 19. Time-averaged rate of change of total mean square slope plotted against time-averaged rate of change of wind speed, all ramp cases.

square slope measurements to bulk values obtained from steady conditions. To reflect this change in the nature of the data, the focus of analysis must shift. Part of that analysis includes computing the cumulative mean square slope (from section 3.1). Shown in Figure 18 is a representation of the change in cumulative mean square slope over the changing wind speed shown in Figure 16. This approach to representing the wavenumber sensitivity of sea surface roughness ties each sea state to its particular wind speed condition, rather than using the simple time progression of the spectrogram. Within Figure 18 is an important piece of information: cumulative mean square slope increases steadily (on semi-log scale) until the high gravity-capillary and

4. Concluding Remarks

The observations described in this paper offer an addition to the body of sea surface wave data that is both scientifically important [Bringer et al., 2013] and useful [Hara et al., 1998]. Results are in agreement with the previously referenced statement from Hwang [2005] (following Jackson et al. [1992], Walsh et al. [1998], and Vandemark et al. [2004]) noting that capillary waves are minor contributors to mean square slope. Results from both sections 3.1 and 3.2, especially those contained within

Figures 14 and 19 appear to strengthen this statement. In all cases and conditions, capillary waves were found to be the weakest contributors to overall surface roughness. Furthermore, capillary waves were found to be the least sensitive to increases in wind speed, strongly implying that such waves reach a level of saturation even at low wind speeds (≈ 3 m/s) and slow wind speed increases (≈ 0.02 m/s²). Gravity-capillary waves, however, were found to be strong contributors to sea surface roughness, both in the stationary (bulk) sense and in the nonstationary (growth) sense. This result further underscores the importance of gravity-capillary waves to processes of momentum transfer between the atmosphere and the ocean.

The Polarimetric Slope Sensing (PSS) technique is a powerful method for measuring the spatial and temporal properties of short-scale waves. Interpreting the polarization of reflected ambient light to obtain sea surface slopes allows for passive, unobtrusive observation of delicate phenomena in an environment that is anything but delicate. The polarimeter is able to resolve waves well into the pure capillary regime without altering their physical properties. Additionally, and importantly, the camera is robust enough to allow acquisition aboard a moving vessel, allowing great latitude in the scientist's directed observational efforts. Other methods of fine-scale wave observation, including the laser slope/elevation gauge setup described in *Donelan et al.* [2010] or the slope-from-refraction technique used in *Jähne and Riemer* [1990] (or more recently, *Kieffer et al.* [2014]) offer high spatial and temporal resolution in the lab, but are not suitable for the field environment.

Field measurements were collected in the northern Gulf of Mexico as part of the GLAD experiment of Summer 2012. The PSS allowed for observation of sea surface waves in the short gravity, gravity-capillary, and capillary regimes. Accompanying these data is a set of wind speed information corresponding to times of wave data acquisition, resulting in a body of data that offers a unique glimpse into the behavior of the air-sea interface under a variety of forcing conditions. A portion of the discussion contained within *Bringer et al.* [2013] described the state of model wave spectra. Specifically, that the disagreement between the energy balance-based spectrum of *Kudryavtsev et al.* [1999], the empirically based spectrum of *Elfouhaily et al.* [1997], and the parameterized spectrum of *Hwang* [2011] call for further wave measurements in the gravity-capillary and pure capillary regimes. The spectra produced from polarimetric observations (and displayed in Figure 12a) are variable in their shape at low winds. Discrepancies in the position of the short-wave peak exist, primarily between the field-obtained spectra of *Yurovskaya et al.* [2013] and the model/parameterized spectra listed previously. In the wind speed range of 5–7 m/s, the polarimetric results contained here seem to agree with the results of *Bringer et al.* [2013] regarding the position of the short wave peak of the saturation spectrum. Specifically, both sources indicate that the peak lies below the 363 rad/m imposed in *Elfouhaily et al.* [1997] and others. Further data acquisition is required to fill gaps in the wind speed record for a more complete comparison between polarimetric results and those of the models/observations listed here. Additionally, the Doppler-shifting effect of background surface current has not been explored; a study similar to this work that incorporates current measurements would add a great deal to the results presented here.

Acquisition of polarimetric imagery aboard the R/V F.G. Walton Smith during the GLAD experiment produced a rich set of information. Great care was placed into quality control; rather than consider the polarimetric data set in its entirety, the authors chose to isolate conditions that would be conducive to producing high-quality data. A focus was placed on consistency; in the style of laboratory-based work, the analysis is focused on stationary and linearly increasing wind speed conditions. It should be reinforced that the majority of the data used here was collected in a small region of time and space, specifically, in the near vicinity of 29° N, 88° W over a period of approximately three days. While this does constrain the data considered to a possibly narrow set of instances, priority was placed in assuring high data fidelity and favorable environmental conditions; the intent of the authors was to discriminate primarily on the basis of wind speed characteristics and not on the properties of the location of acquisition. An important next step would involve repeated, targeted measurements over several areas for a full evaluation of the physical phenomena described.

Acknowledgments

This research was supported in part by a grant from BP/the Gulf of Mexico Research Initiative (SA1207GOMRI005) and grant N000141410643 from the Office of Naval Research. Polarimetric video data and sonic anemometer wind data used in this paper have been archived at GRIIDC (Gulf Research Initiative Information and Data Cooperative, <https://data.gulfresearchinitiative.org>) for future use. Copies of these data may be found through their DOIs: <http://dx.doi.org/10.7266/N7765C77> (meteorological measurements) and <http://dx.doi.org/10.7266/N7X5S595> (slope measurements). Thanks are given to all those who worked on and prepared for the GLAD experiment, in particular Neil Williams and Mike Rebozo. The GLAD experiment would not have been possible without the organization and professionalism of Captain Lake and the crew of the R/V F.G. Walton Smith. The authors are grateful for the model/experimental spectra provided by Paul Hwang, Alexandra Bringer, and Maria Yurovskaya. Insight lent by Will Drennan was helpful in understanding momentum flux. Finally, the authors extend their thanks to three anonymous reviewers who provided constructive comments throughout the revision process.

References

- Bréon, F. M., and N. Henriot (2006), Spaceborne observations of ocean glint reflectance and modeling of wave slope distributions, *J. Geophys. Res.*, *111*, C06005, doi:10.1029/2005JC003343.
- Bringer, A., B. Chapron, A. Mouche, and C.-A. Guérin (2013), Revisiting the short-wave spectrum of the sea surface in the light of the weighted curvature approximation, *IEEE Trans. Geosci. Remote Sens.*, *52*(1), 679–689, doi:10.1109/TGRS.2013.2243459.
- Cauliez, G., and C.-A. Guérin (2012), Higher-order statistical analysis of short wind wave fields, *J. Geophys. Res.*, *117*, C06002, doi:10.1029/2011JC007854.
- Choi, I. (2001), Unit root tests for panel data, *J. Int. Money Finance*, *20*(2), 249–272.
- Cox, C., and W. Munk (1954), Measurement of the roughness of the sea surface from photographs of the sun's glitter, *J. Opt. Soc. Am.*, *44*(11), 838–850.
- Cox, C., and W. Munk (1956), Slopes of the sea surface deduced from photographs of sun glitter, *Bull. Scripps Inst. Oceanogr.*, *6*, 401–488.
- Donelan, M. A., and W. J. Pierson (1987), Radar scattering and equilibrium ranges in wind-generated waves with application to scatterometry, *J. Geophys. Res.*, *92*(C5), 4971–5029.
- Donelan, M. A., W. M. Drennan, and A. K. Magnusson (1996), Nonstationary analysis of the directional properties of propagating waves, *J. Phys. Oceanogr.*, *26*(9), 1901–1914.
- Donelan, M. A., B. K. Haus, W. J. Plant, and O. Troianowski (2010), Modulation of short wind waves by long waves, *J. Geophys. Res.*, *115*, C10003, doi:10.1029/2009JC005794.
- Elfouhaily, T., B. Chapron, K. Katsaros, and D. Vandemark (1997), A unified directional spectrum for long and short wind-driven waves, *J. Geophys. Res.*, *107*(16), 15,781–15,796.
- Frew, N. M. (1997), The role of organic films in air-sea gas exchange, in *The Sea Surface and Global Change*, edited by P. S. Liss, and R. A. Duce, pp. 121–163, Cambridge Univ. Press, Cambridge, U. K.
- Frew, N. M., et al. (2004), Air-sea gas transfer: Its dependence on wind stress, small-scale roughness, and surface films, *J. Geophys. Res.*, *109*, C08S17, doi:10.1029/2003JC002131.
- Hara, T., E. J. Bock, and D. Lyzenda (1994), In situ measurements of capillary-gravity wave spectra using a scanning laser slope gauge and microwave radars, *J. Geophys. Res.*, *99*(C6), 12,593–12,602, doi:10.1029/94JC00531.
- Hara, T., E. J. Bock, J. B. Edson, and W. R. McGillis (1998), Observation of short wind waves in coastal waters, *J. Phys. Oceanogr.*, *28*, 1425–1438, doi:10.1175/1520-0485(1998)028<1425:OOS WWI>2.0.CO;2.
- Hwang, P. A. (2005), Wave number spectrum and mean square slope of intermediate-scale ocean surface waves, *J. Geophys. Res.*, *110*, C10029, doi:10.1029/2005JC003002.
- Hwang, P. A. (2011), A note on the ocean surface roughness spectrum*, *J. Atmos. Oceanic Technol.*, *28*(3), 436–443, doi:10.1175/2010JTECHO812.1.
- Hwang, P. A., S. Atakturk, A. Sletten, and D. B. Trizna (1996), A study of the wave number spectra of short water waves in the ocean, *J. Phys. Oceanogr.*, *26*, 1266–1285, doi:10.1175/1520-0485(1996)026<1266:ASOTWS>2.0.CO;2.
- Högström, U., et al. (2008), Momentum fluxes and wind gradients in the marine boundary layer—a multi-platform study, *Boreal Environ. Res.*, *13*(6), 475–502.
- Jackson, F. C., W. T. Walton, D. E. Hines, B. A. Walter, and C. Y. Peng (1992), Sea surface mean square slope from Ku-band backscatter data, *J. Geophys. Res.*, *97*(C7), 11,411–11,427.
- Jähne, B., and K. S. Riemer (1990), Two-dimensional wave number spectra of small-scale water surface waves, *J. Geophys. Res.*, *11*(C7), 531–546.
- Kieffer, D., S. Reith, and B. Jähne (2014), High-speed imaging of short wind waves by shape from refraction, *J. Eur. Opt. Soc. Rapid Publ.*, *9*.
- Kudryavtsev, V. N., V. K. Makin, and B. Chapron (1999), Coupled sea surface-atmosphere model: 2. Spectrum of short wind waves, *J. Geophys. Res.*, *104*(C4), 7625–7639.
- Munk, W. (2009), An inconvenient sea truth: Spread, steepness, and skewness of surface slopes, *Annu. Rev. Mar. Sci.*, *1*, 377–415, doi:10.1146/annurev.marine.010908.163940.
- Olascoaga, M. J., et al. (2013), Drifter motion in the Gulf of Mexico constrained by altimetric Lagrangian coherent structures, *Geophys. Res. Lett.*, *40*, 6171–6175, doi:10.1002/2013GL058624.
- Phillips, O. M. (1985), Spectral and statistical properties of the equilibrium range in wind-generated gravity waves, *J. Fluid Mech.*, *156*, 505–531.
- Plant, W. J. (1982), A relationship between wind stress and wave slope, *J. Geophys. Res.*, *87*(C3), 1961–1967.
- Poje, A. C., et al. (2014), Submesoscale dispersion in the vicinity of the Deepwater Horizon spill, *Proceedings of the National Academy of Sciences*, *111*(35), 12693–12698.
- Romeiser, R., W. Alpers, and V. Wismann (1997), An improved composite surface model for the radar backscattering cross section of the ocean surface: 1. Theory of the model and optimization/validation by scatterometer data, *J. Geophys. Res.*, *102*(C11), 25,237–25,250.
- Smith, S. D. (1988), Coefficients for sea surface wind stress, heat flux, and wind profiles as a function of wind speed and temperature, *J. Geophys. Res.*, *93*(C12), 15,467–15,472.
- Vandemark, D., B. Chapron, J. Sun, G. H. Crescenti, and H. C. Graber (2004), Ocean wave slope observations using radar backscatter and laser altimeters, *J. Phys. Oceanogr.*, *34*(12), 2825–2842.
- Walsh, E. J., D. C. Vandemark, C. A. Friehe, S. P. Burns, D. Khelif, R. N. Swift, and J. F. Scott (1998), Measuring sea surface mean square slope with a 36-GHz scanning radar altimeter, *J. Geophys. Res.*, *103*(C6), 12,587–12,601.
- Wentz, F. J. (1976), Cox and Munk's sea surface slope variance, *J. Geophys. Res.*, *81*(9), 1607–1608.
- Wright, J. W. (1978), Detection of ocean waves by microwave radar; the modulation of short gravity-capillary waves, *Boundary Layer Meteorol.*, *13*(1–4), 87–105.
- Yurovskaya, M. V., V. A. Dulov, B. Chapron, and V. N. Kudryavtsev (2013), Directional short wind wave spectra derived from the sea surface photography, *J. Geophys. Res. Oceans*, *118*, 4380–4394, doi:10.1002/jgrc.20296.
- Zappa, C. J., M. L. Banner, H. Schultz, A. Corrada-Emmanuel, L. B. Wolff, and J. Yalcin (2008), Retrieval of short ocean wave slope using polarimetric imaging, *Meas. Sci. Technol.*, *19*(13), doi:10.1088/0957-0233/19/5/055503.
- Zappa, C. J., M. L. Banner, H. Schultz, J. R. Gemmrich, R. P. Morison, D. A. LeBel, and T. Dickey (2012), An overview of sea state conditions and air-sea fluxes during RaDyO, *J. Geophys. Res.*, *117*, C00H19, doi:10.1029/2011JC007336.